



1 **An integration of gauge, satellite and reanalysis precipitation datasets**  
2 **for the largest river basin of the Tibetan Plateau**

3 Yuanwei Wang<sup>1,3</sup>, Lei Wang<sup>1,2,3\*</sup>, Xiuping Li<sup>1,2</sup>, Jing Zhou<sup>1</sup>, Zhidan Hu<sup>4</sup>

4 <sup>1</sup> Key Laboratory of Tibetan Environmental Changes and Land Surface Processes,  
5 Institute of Tibetan Plateau Research, Chinese Academy of Sciences, Beijing, China

6 <sup>2</sup> CAS Center for Excellence in Tibetan Plateau Earth Sciences, Beijing, China

7 <sup>3</sup> University of Chinese Academy of Sciences, Beijing, China

8 <sup>4</sup> Information Center, Ministry of Water Resources, Beijing, China

9

10

11

12

13

14

15 Corresponding author:

16 Lei Wang, Dr., Prof.

17 Key Lab. of Tibetan Environmental Changes and Land Surface Processes,

18 Institute of Tibetan Plateau Research, Chinese Academy of Sciences

19 No. 16 Lincui Road, Chaoyang District, Beijing 100101, China

20 Tel: +86-10-84097107 Fax: +86-10-84097079

21 Email: [wanglei@itpcas.ac.cn](mailto:wanglei@itpcas.ac.cn)

22



23 **Abstract:** As the largest river basin of the Tibetan Plateau, the Upper Brahmaputra  
24 River Basin (also called “Yarlung Zangbo” in Chinese) has profound impacts on the  
25 water security of local and downstream inhabitants. Precipitation in the basin is  
26 mainly controlled by the Indian Summer Monsoon and Westerly, and is the key to  
27 understand the water resources available in the basin; however, due to sparse  
28 observational data constrained by a harsh environment and complex topography, there  
29 remains a lack of reliable information on basin-wide precipitation (there are only nine  
30 national meteorological stations with continuous observations). To improve the  
31 accuracy of basin-wide precipitation data, we integrate various gauge, satellite and  
32 reanalysis precipitation datasets, including GLDAS, ITP-Forcing, MERRA2, TRMM  
33 and CMA datasets, to develop a new precipitation product for the 1981-2016 period  
34 over the Upper Brahmaputra River Basin, at 3-hour and 5-km resolution. The new  
35 product has been rigorously validated at different temporal scales (e.g. extreme events,  
36 daily to monthly variability, and long-term trends) and spatial scales (point- and  
37 basin-scale) with gauge precipitation observations, showing much improved  
38 accuracies compared to previous products. An improved hydrological simulation has  
39 been achieved (low relative bias: -5.94%; highest NSE: 0.643) with the new  
40 precipitation inputs, showing reliability and potential for multi-disciplinary studies.  
41 This new precipitation product is openly accessible at  
42 <https://doi.org/10.5281/zenodo.3711155> (Wang et al., 2020) and, additionally at the  
43 National Tibetan Plateau Data Center (<https://data.tpdc.ac.cn>, login required).  
44



45 **1. Introduction**

46 Precipitation plays a very important role in the research of hydrology, meteorology,  
47 ecology, and even social economics, as it is a critical input factor for various models  
48 (e.g. hydrological and land surface models) (Qi et al., 2016; Wang et al., 2017a; Fang  
49 et al., 2019; Miri et al., 2019; Wang et al., 2019a). Specifically, precipitation is a key  
50 part of the water balance and energy cycle and will directly impact runoff generation  
51 and soil moisture movement (Su et al., 2008). As a result, water resource management  
52 tasks such as flood forecasting and drought monitoring, ecological environment  
53 restoration (e.g. vegetation growth and protection), and many other scientific and  
54 social applications are closely linked with precipitation patterns (Funk et al., 2015).

55 The Tibetan Plateau (TP), known as the highest plateau in the world, is covered by  
56 massive glaciers, snow and permafrost, which significantly affect the hydrological  
57 processes of all the large rivers that are fed by it; the Brahmaputra, the Salween, and  
58 the Mekong, among others. Therefore, it is necessary to explore the hydrological  
59 variations over the TP to achieve efficient utilization and protection of its water  
60 resources and a better understanding of the effects of climate change on the  
61 surrounding region. However, due to the irregular and sparse distribution of national  
62 meteorological stations, particularly in the Upper Brahmaputra (precipitation data  
63 from only nine stations are available, and are sparsely distributed; see Sang et al.,  
64 2016; Cuo et al., 2019), there are large data constraints on research on these  
65 hydrological processes and their responses to climate change. Although there are  
66 many more rain gauges managed by the Ministry of Water Resources (MWR), most



67 of them are located in middle-stream regions and rainfall datasets are only recorded  
68 over short time periods. Simply using the linear mean of these station observations to  
69 calculate variations in precipitation for the entire basin is impractical and prone to  
70 problems (Lu et al., 2015). Accurate spatial distributions of precipitation are  
71 unavailable. This influences the generation of historical runoff data (Mazzoleni et al.,  
72 2019), meaning that the specific contributions of glaciers, snow cover, permafrost and  
73 vegetation to hydrological processes in this area cannot be analyzed and quantified,  
74 posing a threat to regional sustainable development and living conditions (Shen et al.,  
75 2010; Guo et al., 2016; Kidd et al., 2017; Shi et al., 2017; Ruhi et al., 2018; Sun et al.,  
76 2018).

77 A longer time series of spatially consistent and temporally continuous  
78 precipitation products could be used to improve our understanding of feedback  
79 mechanisms between different meteorological and hydrological components,  
80 especially under the background signal of climate change. Various satellite rainfall  
81 products have been widely used in previous studies, such as the National Oceanic and  
82 Atmospheric Administration/Climate Prediction Centre (NOAA/CPC) morphing  
83 technique (CMORPH) (Ferraro et al., 2000; Joyce et al., 2004), and the Tropical  
84 Rainfall Measuring Mission (TRMM) (Huffman et al., 2007). However, there are still  
85 problems in estimating daily (Meng et al., 2014; Bai and Liu, 2018) and extreme  
86 precipitation (Funk et al., 2015; Zhou et al., 2015b; Fang et al., 2019), especially in  
87 mountainous regions with high elevations and fewer ground measurements, such as  
88 the Upper Brahmaputra (Xia et al., 2015; Xu et al., 2017; Qi et al., 2018). Additionally,



89 there are several reanalysis datasets that have been widely used by researchers, such  
90 as the Global Land Data Assimilation System (GLDAS) (Rodell et al., 2004; Zaitchik  
91 et al., 2010; Wang et al., 2011) and the Modern-Era Retrospective analysis for  
92 Research and Applications, Version 2 (MERRA2) dataset (Gelaro et al., 2017; Reichle  
93 et al., 2017a, 2017b). Evaluation of GLDAS data has generally been limited to the  
94 United States and other regions with adequate ground observations (Kato et al., 2007;  
95 Qi et al., 2016). Most studies have focused on evapotranspiration, soil moisture and  
96 groundwater products derived from GLDAS or MERRA2 (Bibi et al., 2019; Deng et  
97 al., 2019; Li et al., 2019a); meanwhile, to the best of our knowledge, there has been  
98 less focus on the evaluation of methods of precipitation estimation and little work on  
99 the corresponding river discharge simulations within the Upper Brahmaputra River  
100 Basin. These precipitation products generally have the advantage of wide and  
101 consistent coverage and have shown great potential in many applications (Li et al.,  
102 2015; Zhang et al., 2017; Fang et al., 2019), but also suffer from large uncertainties  
103 over the Upper Brahmaputra River Basin due to indirect observations, insufficient  
104 gauge calibration, and complex topography (Tong et al., 2014; Yong et al., 2015; Xu  
105 et al., 2017).

106 In this study, we focus on integrating gauge, satellite and reanalysis precipitation  
107 datasets to generate a new dataset over the Upper Brahmaputra, suitable for use in  
108 hydrological simulations and other scientific researches related to climate change. The  
109 remainder of this study is structured as follows. Section 2 briefly describes the study  
110 area, datasets, and methodology used. Section 3 presents and discusses the evaluation



111 results of different products and validates the accuracy and reliability of our integrated  
112 dataset. Then Section 4 is the data availability. Finally, conclusions are given in  
113 Section 5.

## 114 **2. Materials and Methods**

### 115 **2.1. Study Area**

116 This study is conducted in Upper Brahmaputra River Basin (27°-32°N, 81°-98°E)  
117 located in the south of the Tibetan Plateau (Figure 1). The Brahmaputra River is an  
118 important part of the whole GBM basin (Ganges, Brahmaputra, Meghna) which  
119 significant influences the natural resources and social development of the Tibetan  
120 Plateau and South Asia. The river is approximately 2,057 km long with a drainage  
121 area of 240,000 km<sup>2</sup>. The climatic conditions are complicated by the extremely high  
122 altitude and highly varying topography (Wang et al., 2018; Wang et al., 2019b);  
123 elevation varies by up to 6,500 m throughout the study region. Generally, the  
124 intra-annual distribution of precipitation is extremely uneven, with more precipitation  
125 distributed in the warm seasons (Wang et al., 2019a). Since the Indian and East Asian  
126 monsoons bring more water vapor in summer and the westerlies dominate in winter  
127 (Yi et al., 2013; Wang et al., 2018; Li et al., 2019a, 2019b), there is a declining trend  
128 of precipitation from the humid southeast to the arid northwest, on average. In recent  
129 decades, the TP has been experiencing a significant warming trend exceeding that in  
130 the Northern Hemisphere (Liu and Chen, 2000; Yang et al., 2014), which will affect  
131 the generation and distribution of precipitation and influence hydrological processes  
132 throughout the Upper Brahmaputra.



## 133 2.2. Datasets

134 Monthly precipitation data (1981-2016) from nine meteorological stations were  
135 obtained from the China Meteorological Administration (CMA), and daily  
136 precipitation data (May to October in 2014 and 2016) from 166 rain gauges were  
137 accessed through the Ministry of Water Resources (MWR), China (Figure 1). Both of  
138 these are regarded as observed precipitation data. Daily river discharge data at Nuxia  
139 station (Figure 1) are used to assess the simulation performance when forced by  
140 different precipitation products.

141 In this study, we chose five types of satellite and reanalysis precipitation products  
142 (Table 1). We, first, evaluated their performance at detecting precipitation, and second,  
143 integrated them to generate a better product, designed to enhance the strengths of each  
144 product.

145 The three satellite and reanalysis data products, GLDAS, MERRA2 and TRMM,  
146 were acquired from the National Aeronautics and Space Administration (NASA)  
147 website (<https://disc.gsfc.nasa.gov/>). GLDAS ingests satellite- and ground-based  
148 observational data products and applies advanced land surface modeling and data  
149 assimilation techniques (Rodell et al., 2004; Zaitchik et al., 2010; Xia et al., 2019); it  
150 has been widely used for river discharge simulations, groundwater monitoring and  
151 many other fields (Wang et al., 2011; Chen et al., 2013; Qi et al., 2018; Verma and  
152 Katpatal, 2019). MERRA2 is the first long-term global reanalysis dataset to assimilate  
153 space-based observations of aerosols and represent their interactions alongside other  
154 physical processes in the climate system (Marquardt Collow et al., 2016; Reichle et al.,



155 2017a, 2017b), and TRMM is a joint mission between the NASA and the Japan  
156 Aerospace Exploration Agency (JAXA) to study rainfall for weather and climate  
157 research (Xu et al., 2017; Ali et al., 2019; Wang et al., 2019a). The ITP-Forcing  
158 dataset has been developed by the hydrometeorological research group at the Institute  
159 of Tibetan Plateau Research, Chinese Academy of Sciences (He, 2010), and has been  
160 shown to perform well on the TP (Yang et al., 2010; Chen et al., 2011). These data  
161 were downloaded from the Cold and Arid Regions Science Data Center  
162 (<http://westdc.westgis.ac.cn/>).

### 163 **2.3. Methods**

164 In this study, because of the different spatial resolutions of different products, we  
165 extracted the precipitation values from each product according to the locations of the  
166 gauges to generate product-gauge data pairings for evaluation. Where there are at least  
167 two gauges in the pixel of one product, we used the average value of the gauges to  
168 evaluate the performance of the corresponding precipitation product data.

169 To ensure the consistency of different products, we interpolated all the products  
170 into the same 5 km spatial resolution grid using the inverse distance weighted (IDW)  
171 method (Ma et al., 2019; Qiao et al., 2019; Sangani et al., 2019) and calculated them  
172 at 3-hourly resolution. Due to its good performance on the TP, we then used the  
173 ITP-Forcing data (1981-2016) to derive the multi-year mean 3-hour data as  
174 background climatological precipitation. Then, the precipitation anomalies between  
175 CMA, GLDAS, ITP-Forcing, MERRA2, TRMM and the background were calculated  
176 3-hourly, using:





$$\begin{aligned} \varepsilon_c &= P_C - P_B \\ \varepsilon_g &= P_G - P_B \\ \varepsilon_i &= P_I - P_B \\ \varepsilon_m &= P_M - P_B \\ \varepsilon_t &= P_T - P_B \end{aligned} \quad (1)$$

177 where  $P_B$ ,  $P_C$ ,  $P_G$ ,  $P_I$ ,  $P_M$ ,  $P_T$  represent the background precipitation and different  
178 products, respectively, and  $\varepsilon$  denotes the corresponding precipitation anomalies.  
179 Considering different weights for these anomalies, we combined the background  
180 precipitation with these anomalies,  
181

$$182 \quad P_{int} = P_B + w_1\varepsilon_c + w_2\varepsilon_g + w_3\varepsilon_i + w_4\varepsilon_m + w_5\varepsilon_t \quad (2)$$

183 where  $w$  represents the weight for each anomaly and  $P_{int}$  refers to the new integrated  
184 precipitation at 5 km and 3-hourly resolution.

185 After  $P_{int}$  was acquired, we corrected its probability distribution function (PDF)  
186 based on the rain gauges, and undertook several validation steps for spatial  
187 distribution and at different time scales (e.g. extreme events, seasonal to inter-annual  
188 variability, and long-term trends). At the same time, we also analyzed the changing  
189 trend over the 36 years, and the extremely high precipitation events during the warm  
190 months in 2014 and 2016. In order to identify the extreme events, we first assumed  
191 that daily precipitation conforms to a normal distribution. From this we calculated a  
192 threshold, above which the probability of precipitation values occurring is less than  
193 0.05 (e.g. Fang et al., 2019 use 0.1). We considered events with precipitation values  
194 above this threshold as extreme events.

$$195 \quad P(\text{precipitation} \geq \text{threshold}) \leq 0.05 \quad (3)$$

196 where  $P$  denotes the probability. Finally, based on the observed discharge data at



197 Nuxia Station, we compared the simulated daily discharges (normalized) from 2008 to  
198 2016 using a water and energy budget-based distributed hydrological model  
199 (WEB-DHM) to check the accuracy and reliability of our integrated precipitation.  
200 Evaluation criteria used in the discharge error assessment include relative bias (RB)  
201 and the Nash-Sutcliffe coefficient of efficiency (NSE).

$$202 \quad Q_{normalized} = \frac{Q - \min Q_{obs}}{\max Q_{obs} - \min Q_{obs}} \quad (4)$$

$$203 \quad RB = \frac{\sum_{i=1}^n Q_{sim} - \sum_{i=1}^n Q_{obs}}{\sum_{i=1}^n Q_{obs}} \times 100\% \quad (5)$$

$$204 \quad NSE = 1 - \frac{\sum_{i=1}^n (Q_{obs} - Q_{sim})^2}{\sum_{i=1}^n (Q_{obs} - \overline{Q_{obs}})^2} \quad (6)$$

205 Where  $Q_{normalized}$ ,  $Q_{obs}$ ,  $Q_{sim}$  represent the normalized discharge, observed discharge,  
206 and simulated discharge, respectively. The perfect value of  $RB$  is 0 and that of  $NSE$  is  
207 1. More information about this model can be found in many studies (Wang et al., 2009;  
208 Wang and Koike, 2009; Xue et al., 2013; Zhou et al., 2015a; Wang et al., 2016; Wang  
209 et al., 2017a). Figure 2 shows the flowchart of this study and Figure 3 presents the  
210 final spatial distribution of our integrated product.

### 211 **3. Results and Discussion**

#### 212 **3.1. Evaluation of precipitation products at the basin and grid scale**

213 Figures 4 and 5 analyze the overall regime of different precipitation products at  
214 the basin scale. Figure 4 is the spatial distribution in warm (May to Oct.) and cold  
215 (Nov. to Apr.) months, and Figure 5 presents the time series of basin-averaged annual



216 and monthly precipitation values. The spatial pattern indicates that more precipitation  
217 occurs in warm seasons and less in cold seasons. During the warm months, GLDAS  
218 and TRMM present obvious regional differences between upstream and downstream,  
219 while CMA gridded data show the lesser values in the upstream source region. In the  
220 cold seasons, all products present almost the same pattern, among which MERRA2  
221 gives the lowest precipitation values.

222 For annual precipitation, CMA, ITP-Forcing and MERRA2 show similar  
223 characteristics (annual mean value: 615 mm, 550 mm and 506 mm, respectively),  
224 while GLDAS and TRMM are 789 mm and 757 mm, respectively. There are also  
225 significant ( $p < 0.01$ ) increasing trends in annual precipitation of GLDAS,  
226 ITP-Forcing, and MERRA2 (6.42, 3.28, 4.68 mm/year, respectively) over the 36 years  
227 of the data. For monthly precipitation, GLDAS and TRMM greatly overestimate  
228 summer precipitation compared to the others, which explains why these two products  
229 give anomalously high annual values (nearly 200 mm greater than the other three data  
230 products). On the other hand, the monthly variations indicate that the intra-annual  
231 distribution of precipitation is extremely uneven.

232 Figures 6 and 7 compare the accuracy of monthly rainfall from different products  
233 at the grid scale. Due to the coarse spatial resolution of MERRA2 ( $0.5^\circ \times 0.625^\circ$ ), there  
234 are fewer product-gauge data pairings available for evaluation. All the products show  
235 similar correlation relationships with the observations, with most rain gauges  
236 overestimating monthly precipitation (Figure 7). The highest correlation coefficient is  
237 0.63 (MERRA2) and the lowest is 0.51 (GLDAS). The PDFs, however, show



238 different characteristics (Figure 6). The CMA data are more consistent with the gauge  
239 data, while GLDAS and TRMM exhibit clear overestimations. As for ITP-Forcing, its  
240 precipitation is more concentrated on the average value, as indicated by the narrow  
241 curve.

## 242 **3.2. Integration of precipitation products and validation of $P_{int}$**

### 243 **3.2.1. Integration of precipitation products and validation against different time** 244 **series**

245 Figure 3 presents the spatial distribution of annual and seasonal precipitation  
246 estimated by our integrated dataset, which shows a declining trend from the southeast  
247 to northwest. Figure 5 then compares the monthly and annual precipitation calculated  
248 from our integrated dataset with the satellite and reanalysis products. As discussed in  
249 Section 2.3, we interpolated all the products into a spatial resolution of 5 km using the  
250 IDW method, and calculated them at a temporal resolution of 3 hours. Comparing  
251 different weights for the anomalies mentioned in Equation 2, we finally adopted the  
252 same weight for each product ( $w = 1/3$  from 1981 to 1997;  $w = 0.25$  from 1998 to  
253 2007;  $w = 0.2$  from 2008 to 2016) to develop the new product, then corrected its PDF  
254 based on the rain gauge data (Figure 6).

255 After  $P_{int}$  was derived, we first validated its performance against short time  
256 series (Figure 8).  $P_{int}$  shows optimal performance at detecting daily precipitation  
257 with the correlation coefficients of 0.43 in 2014 and 0.55 in 2016. In 2014, the  
258 average bias is 0.20 mm and the root mean square error (RMSE) is 4.18 mm.  $P_{int}$   
259 successfully captures the daily variation of precipitation except for late September and



260 early October. For 2016, the average bias and RMSE are -0.006 mm and 2.62 mm,  
261 respectively, much better than those for 2014.

262 We then check the spatial distribution of  $P_{int}$  from May to October in 2014 and  
263 2016 (Figure 9). Every rain gauge is compared with its corresponding grid in  $P_{int}$  to  
264 explore the spatial heterogeneity.  $P_{int}$  well reproduces the precipitation pattern  
265 described by less rain in the upstream (western) regions and more rain in the  
266 downstream (eastern) regions. Meanwhile, abundant rainfall occurs in summer,  
267 particularly for July.

268 Building on this, further validation was undertaken against a long time series. We  
269 chose the average monthly precipitation from the nine meteorological stations as the  
270 evaluation standard against which to assess  $P_{int}$  (Figure 10). The PDF of  $P_{int}$  is  
271 consistent with that of the station data, which indicates that the mean value and  
272 standard deviation of  $P_{int}$  are much closer to the observed value (Figure 10a).  
273 Similar to the short time series, the average bias (-4.50 mm) and the RMSE (13.6 mm),  
274 especially with respect to the correlation coefficient (0.96), prove that the  $P_{int}$  is  
275 applicable and reliable.

### 276 **3.2.2. Trend and extreme events analysis compared across different precipitation** 277 **products**

278 The trend analysis (Figure 11) over 36 years indicates that there are different  
279 patterns of precipitation in different seasons and different regions. In summer, there  
280 are more complicated trends, as the variations between up and down stream differ  
281 greatly. On the contrary, trends of winter precipitation values over most of the study



282 region vary by merely  $\pm 2$  mm/year, illustrating that precipitation in winter generally  
283 remains unchanged or experiences minimal change. To find if  $P_{int}$  is able to reflect  
284 the true varying trend, we added a comparison between meteorological stations  
285 (triangles in Figure 11 and their direction represent the true trend) and precipitation  
286 products. For observed annual precipitation, all the stations give an insignificant  
287 increasing trend, except for Bomi station, which is located in the easternmost part of  
288 the study region. For seasonal precipitation, different stations present different  
289 patterns. As a result,  $P_{int}$  appears to reflect the changing pattern of more stations  
290 than any other product, with the exception of the ITP-Forcing dataset on an annual  
291 timescale or over autumn (Figure 12).

292 We notice that there is increasing trend in annual precipitation almost in the  
293 whole basin for  $P_{int}$ ; only precipitation in the midstream area near the Himalaya  
294 mountains and small part of the upstream region are decreasing. Moreover, the  
295 majority of the increased precipitation in the downstream regions occurs over spring  
296 and summer, with only slight changes found in autumn and winter.

297 After the volume, the spatial distribution, and the trend of  $P_{int}$  at different time  
298 scales were completely verified, we continued to inspect if  $P_{int}$  could capture the  
299 extreme events from May to October in 2014 and 2016 according to the rain gauge  
300 data (Figure 13). There are 27 days in total (19 days in 2014 and 8 days in 2016)  
301 when extremely high daily precipitation occurred. All the products are comparable  
302 with each other in underestimating the frequency of extreme events. Nine days are  
303 identified out of the  $P_{int}$  data, lesser only to the number of days detected by



304 ITP-Forcing (11 days).

305 **3.2.3. Evaluation of daily discharges simulated by different precipitation**  
306 **products**

307 All the comparison and validation steps undertaken above support the accuracy  
308 and reliability of our integrated dataset. Furthermore, Figure 14 indicates the superior  
309 suitability and application of  $P_{int}$  in hydrological simulation and investigation, with  
310 an RB of -5.94% and an NSE of 0.643 (the highest). We simulate the daily discharge  
311 of Nuxia station using the various precipitation datasets as the input with the same  
312 initial conditions and physical parameters. All products overestimate the daily  
313 discharge, except for  $P_{int}$  (-5.94%) and MERRA2 (-2.24%). In terms of NSE,  $P_{int}$   
314 (0.643), ITP-Forcing (0.543) and MERRA2 (0.544) are higher than others, explaining  
315 their better simulation performance. GLDAS and TRMM offer the worst performance  
316 in discharge simulation, which is consistent with their overestimation of precipitation  
317 in summer (Figure 5). This indicates that these datasets should be corrected when  
318 undertaking hydrological research over the Upper Brahmaputra.

319 **4. Data availability**

320 This high spatiotemporal resolution (5km, 3h) precipitation dataset over the  
321 Upper Brahmaputra River Basin from 1981 to 2016 is freely available at  
322 <https://doi.org/10.5281/zenodo.3711155> (Wang et al., 2020), which can be  
323 downloaded in TXT format.

324 **5. Conclusion**

325 In order to acquire suitable and accurate precipitation datasets which are helpful



326 in hydrology, meteorology and other scientific research over the Upper Brahmaputra,  
327 we produced a new precipitation product by integrating gauge, satellite and reanalysis  
328 precipitation datasets to reduce the uncertainties associated with a single product and  
329 limitation of few observation stations. Our integrated dataset performs better than the  
330 input datasets in estimating daily and monthly precipitation, describing the spatial  
331 heterogeneity, capturing variation trends and extreme events and simulating river  
332 discharges. Furthermore, it is successful in reproducing daily precipitation variation,  
333 with smaller average biases (0.2 mm in 2014 and -0.006 mm in 2016) and RMSE  
334 values (4.18 mm in 2014 and 2.62 mm in 2016). Monthly precipitation shows higher  
335 correlation coefficients with the in-situ data for various time series (0.69 for all the  
336 rain gauges in the warm months of 2014 and 2016; 0.86 for the nine meteorological  
337 stations over 1981-2016). This high spatio-temporal resolution assures us that we can  
338 use this new dataset to explore more detailed physical processes and further  
339 understand the impacts of climate change on the water resources of the Upper  
340 Brahmaputra River Basin, and we are confident that our precipitation dataset will  
341 greatly assist future research in this basin.

342 With this in mind, we note some aspects of this study that deserve further  
343 consideration. The effect of altitude on precipitation has not been taken into account  
344 in the development of this dataset. We also note uncertainties that may arise from the  
345 re-gridding of the remotely sensed datasets in order to pair with the in-situ gauge data.  
346 In addition, the assumption of normal distribution when analyzing extremely high  
347 daily precipitation can also lead to uncertainty. This study provides a foundation from





348 which to explore these aspects in more detail.

349 In the future, more studies are needed to validate the method and data in regions  
350 with complex topography and climatic conditions, and to further improve the retrieval  
351 algorithm. This will greatly benefit hydrological applications, especially in areas with  
352 sparse and irregular observation networks. Furthermore, no products used in this  
353 study accurately represent extreme precipitation events, thus, it is necessary to  
354 improve the ability of all of these products to capture extreme events.

#### 355 **Acknowledgments**

356 This study was financially supported by the National Natural Science Foundation  
357 of China (Grant No. 91747201) and the Strategic Priority Research Program of  
358 Chinese Academy of Sciences (Grant No. XDA20060202 and XDA19070301). Jing  
359 Zhou was supported by the National Natural Science Foundation of China (Grant No.  
360 41771089). The Shuttle Radar Topographic Mission (SRTM) Digital Elevation Model  
361 (DEM), with a ground resolution of 30 m, is available from the United States  
362 Geological Survey's (USGS) web portal ([www.earthexplorer.usgs.gov](http://www.earthexplorer.usgs.gov)). We would  
363 also like to thank NASA for different precipitation data including GLDAS, MERRA2,  
364 TRMM (<https://disc.gsfc.nasa.gov/>). Lastly, we are pleased to acknowledge the  
365 anonymous reviewers and editor's valuable comments and suggestions to improve  
366 this manuscript.

#### 367 **Conflicts of Interest**

368 The authors declare no conflicts of interest.

#### 369 **References**



- 370 Ali, S., Tong, D., Xu, Z., Henchiri, M., Wilson, K., Shi, S., and Zhang, J.:  
371 Characterization of drought monitoring events through MODIS- and  
372 TRMM-based DSI and TVDI over south Asia during 2001–2017, *Environ. Sci.*  
373 *Pollut. Res.*, 26(32), 33568-33581, 2019.
- 374 Bai, P., and Liu, X.: Evaluation of Five Satellite-Based Precipitation Products in Two  
375 Gauge-Scarce Basins on the Tibetan Plateau, *Remote Sens.*, 10(8), 1316, 2018.
- 376 Bibi, S., Wang, L., Li, X., Zhang, X., and Chen, D.: Response of groundwater storage  
377 and recharge in the Qaidam Basin (Tibetan Plateau) to climate variations from  
378 2002 to 2016, *J. Geophys. Res.: Atmos.*, 124(17-18), 9918-9934, 2019.
- 379 Chen, Y., Yang, K., He, J., Qin, J., Shi, J., Du, J., and He, Q.: Improving land surface  
380 temperature modeling for dry land of China, *J. Geophys. Res.: Atmos.*, 116(D20),  
381 2011.
- 382 Chen, Y., Yang, K., Qin, J., Zhao, L., Tang, W., and Han, M.: Evaluation of AMSR-E  
383 retrievals and GLDAS simulations against observations of a soil moisture  
384 network on the central Tibetan Plateau, *J. Geophys. Res.: Atmos.*, 118(10),  
385 4466-4475, 2013.
- 386 Cuo, L., Li, N., Liu, Z., Ding, J., Liang, L., Zhang, Y., and Gong, T.: Warming and  
387 human activities induced changes in the Yarlung Tsangpo basin of the Tibetan  
388 plateau and their influences on streamflow, *J. Hydrol.: Regional Studies*, 25,  
389 100625, 2019
- 390 Deng, M., Meng, X., Li, Z., Lyv, Y., Lei, H., Zhao, L., Zhao, S., Ge, J., and Jing, H.:  
391 Responses of soil moisture to regional climate change over the Three Rivers



- 392 Source Region on the Tibetan plateau, *Int. J. Climatol.*, 1-15, 2019.
- 393 Fang, J., Yang, W., Luan, Y., Du, J., Lin, A., and Zhao, L.: Evaluation of the TRMM  
394 3B42 and GPM IMERG products for extreme precipitation analysis over China,  
395 *Atmos. Res.*, 223, 24-38, 2019.
- 396 Ferraro, R.R., Weng, F., Grody, N.C., and Zhao, L.: Precipitation characteristics over  
397 land from the NOAA-15 AMSU sensor, *Geophys. Res. Lett.*, 27(17), 2669-2672,  
398 2000.
- 399 Funk, C., Peterson, P., Landsfeld, M., Pedreros, D., Verdin, J., Shukla, S., Husak, G.,  
400 Rowland, J., Harrison, L., Hoell, A., and Michaelsen, J.: The climate hazards  
401 infrared precipitation with stations-a new environmental record for monitoring  
402 extremes, *Sci. Data*, 2(1), 1-21, 2015.
- 403 Gelaro, R., McCarty, W., Suárez, M.J., Todling, R., Molod, A., Takacs, L., Randles,  
404 C.A., Darmenova, A., Bosilovicha, M.G., Reichlea, R., Wargan, K., Coya, L.,  
405 Cullather, R., Draper, C., Akella, S., Buchard, V., Conaty, A., Silva, A.M., Gu,  
406 W., Kima, G-K., Koster, R., Lucchesi, R., Merkova, D., Nielsen, J.E., Partyka,  
407 G., Pawsona, S., Putman, W., Rienecker, M., Schubert, S.D., Sienkiewicz, M.,  
408 and Zhao, B.: The modern-era retrospective analysis for research and  
409 applications, version 2 (MERRA-2), *J. Clim.*, 30(14), 5419-5454, 2017.
- 410 Guo, H., Chen, S., Bao, A., Behrangi, A., Hong, Y., Ndayisaba, F., Hu, J., and  
411 Stepanian, P.M.: Early assessment of integrated multi-satellite retrievals for  
412 global precipitation measurement over China, *Atmos. Res.*, 176, 121-133, 2016.
- 413 He, J.: Development of surface meteorological dataset of China with high temporal



- 414 and spatial resolution, Master dissertation, Institute of Tibetan Plateau Research,  
415 Chinese Academy of Science, 2010.
- 416 Huffman, G.J., Adler, R.F., Rudolf, B., Schneider, U., and Keehn, P.R.: Global  
417 precipitation estimates based on a technique for combining satellite-based  
418 estimates, rain gauge analysis, and NWP model precipitation information, *J.*  
419 *Clim.*, 8(5), 1284-1295, 1995.
- 420 Huffman, G.J., Bolvin, D.T., Nelkin, E.J., Wolff, D.B., Adler, R.F., Gu, G., Hong, Y.,  
421 Bowman, K.P., and Stocker, E.F.: The TRMM multisatellite precipitation  
422 analysis (TMPA): Quasi-global, multiyear, combined-sensor precipitation  
423 estimates at fine scales, *J. Hydrometeorol.*, 8(1), 38-55, 2007.
- 424 Joyce, R.J., Janowiak, J.E., Arkin, P.A., and Xie, P.: CMORPH: A method that  
425 produces global precipitation estimates from passive microwave and infrared  
426 data at high spatial and temporal resolution, *J. Hydrometeorol.*, 5(3), 487-503,  
427 2004.
- 428 Kato, H., Rodell, M., Beyrich, F., Cleugh, H., Gorsel, E.V., Liu, H., and Meyers, T.P.:  
429 Sensitivity of land surface simulations to model physics, land characteristics, and  
430 forcings, at four CEOP sites, *J. Meteorol. Soc. Jpn.*, 85, 187-204, 2007.
- 431 Kidd, C., Becker, A., Huffman, G.J., Muller, C.L., Joe, P., Skofronick-Jackson, G.,  
432 and Kirschbaum, D.B.: So, how much of the Earth's surface is covered by rain  
433 gauges?, *Bull. Am. Meteorol. Soc.*, 98(1), 69-78, 2017.
- 434 Li, X., Long, D., Han, Z., Scanlon, B.R., Sun, Z., Han, P., and Hou, A.:  
435 Evapotranspiration Estimation for Tibetan Plateau Headwaters using Conjoint



- 436 Terrestrial and Atmospheric Water Balances and Multisource Remote Sensing,  
437 Water Resour. Res., 55, <https://doi.org/10.1029/2019WR025196>, 2019a.
- 438 Li, X., Long, D., Huang, Q., Han, P., Zhao, F., and Wada, Y.:  
439 High-temporal-resolution water level and storage change data sets for lakes on  
440 the Tibetan Plateau during 2000–2017 using multiple altimetric missions and  
441 Landsat-derived lake shoreline positions, Earth Syst. Sci. Data, 11(4), 1603-1627,  
442 2019b.
- 443 Li, Z., Yang, D., Gao, B., Jiao, Y., Hong, Y., and Xu, T.: Multiscale hydrologic  
444 applications of the latest satellite precipitation products in the Yangtze River  
445 Basin using a distributed hydrologic model, J Hydrometeorol., 16(1), 407-426,  
446 2015.
- 447 Liu, X., and Chen, B.: Climatic warming in the Tibetan Plateau during recent decades,  
448 Int. J. Climatol., 20(14), 1729-1742, 2000.
- 449 Lu, N., Trenberth, K.E., Qin, J., Yang, K., and Yao, L.: Detecting long-term trends in  
450 precipitable water over the Tibetan Plateau by synthesis of station and MODIS  
451 observations, J. Clim., 28(4), 1707-1722, 2015.
- 452 Ma, J., Ding, Y., Cheng, J.C.P., Jiang, F., and Wan, Z.: A temporal-spatial  
453 interpolation and extrapolation method based on geographic Long Short-Term  
454 Memory neural network for PM 2.5, J. Cleaner Prod., 237, 117729, 2019.
- 455 Marquardt Collow, A.B., Bosilovich, M.G., and Koster, R.D.: Large-scale influences  
456 on summertime extreme precipitation in the northeastern United States, J.  
457 Hydrometeorol., 17(12), 3045-3061, 2016.



- 458 Mazzoleni, M., Brandimarte, L., and Amaranto, A.: Evaluating precipitation datasets  
459 for large-scale distributed hydrological modelling, *J. Hydrol.*, 578, 124076, 2019.
- 460 Meng, J., Li, L., Hao, Z., Wang, J., and Shao, Q.: Suitability of TRMM satellite  
461 rainfall in driving a distributed hydrological model in the source region of  
462 Yellow River, *J. Hydrol.*, 509, 320-332, 2014.
- 463 Miri, M., Masoudi, R., and Raziqi, T.: Performance Evaluation of Three  
464 Satellites-Based Precipitation Data Sets Over Iran, *J. Indian Soc. Remot.*, 47(12),  
465 2073-2084, 2019.
- 466 Qi, W., Liu, J., and Chen, D.: Evaluations and improvements of GLDAS2.0 and  
467 GLDAS2.1 forcing data's applicability for basin scale hydrological simulations  
468 in the Tibetan Plateau, *J. Geophys. Res.: Atmos.*, 123(23), 13,128-13,148, 2018.
- 469 Qi, W., Zhang, C., Fu, G., Sweetapple, C., and Zhou, H.: Evaluation of global  
470 fine-resolution precipitation products and their uncertainty quantification in  
471 ensemble discharge simulations, *Hydrol. Earth Syst. Sci.*, 20(2), 903-920, 2016.
- 472 Qi, W., Zhang, C., Fu, G., and Zhou H.: Global Land Data Assimilation System data  
473 assessment using a distributed biosphere hydrological model, *J. Hydrol.*, 528,  
474 652-667, 2015.
- 475 Qiao, P., Li, P., Cheng, Y., Wei, W., Yang, S., Lei, M., and Chen, T.: Comparison of  
476 common spatial interpolation methods for analyzing pollutant spatial  
477 distributions at contaminated sites, *Environ. Geochem. Health*, 41, 2709-2730,  
478 2019.
- 479 Rasouli, K., Pomeroy, J.W., Janowicz, J.R., Williams, T.J., and Carey, S.K.: A



480 long-term hydrometeorological dataset (1993–2014) of a northern mountain  
481 basin: Wolf Creek Research Basin, Yukon Territory, Canada, *Earth Syst. Sci.*  
482 *Data*, 11(1), 89-100, 2019.

483 Reichle, R.H., Draper, C.S., Liu, Q., Girotto, M., Mahanama, S.P.P., Koster, R.D.,  
484 and De Lannoy, G.J.M.: Assessment of MERRA-2 land surface hydrology  
485 estimates, *J. Clim.*, 30(8), 2937-2960, 2017a.

486 Reichle, R.H., Liu, Q., Koster, R.D., Draper, C.S., Mahanama, S.P.P., and Partyka,  
487 G.S.: Land surface precipitation in MERRA-2, *J. Clim.*, 30(5), 1643-1664,  
488 2017b.

489 Roca, R., Alexander, L.V., Potter, G., Bador, M., Juca, R., Contractor, S., Bosilovich,  
490 M.G., and Cloche, S.: FROGS: a daily  $1^\circ \times 1^\circ$  gridded precipitation database of  
491 rain gauge, satellite and reanalysis products, *Earth Syst. Sci. Data*, 11(3),  
492 1017-1035, 2019.

493 Rodell, M., Houser, P.R., Jambor, U., Gottschalck, J., Mitchell, K., Meng, C-J.,  
494 Arsenault, K., Cosgrove, B., Radakovich, J., Bosilovich, M., Entin, J.K., Walker,  
495 J.P., Lohmann, D., and Toll, D.: The Global Land Data Assimilation System,  
496 *Bull. Am. Meteorol. Soc.*, 85(3), 381-394, 2004.

497 Rodell, M., McWilliams, E.B., Famiglietti, J.S., Beaudoin, H.K., and Nigro, J.:  
498 Estimating evapotranspiration using an observation based terrestrial water budget,  
499 *Hydrol. Processes*, 25(26), 4082-4092, 2011.

500 Ruhi, A., Messenger, M.L., and Olden, J.D.: Tracking the pulse of the Earth's fresh  
501 waters, *Nature Sustainability*, 1(4), 198-203, 2018.



- 502 Sang, Y., Singh, V.P., Gong, T., Xu, K., Sun, F., Liu, C., Liu, W., and Chen, R.:  
503 Precipitation variability and response to changing climatic condition in the  
504 Yarlung Tsangpo River basin, China, *J. Geophys. Res.: Atmos.*, 121, 8820–8831,  
505 doi:10.1002/2016JD025370, 2016.
- 506 Sangani, M.F., Khojasteh, D.N., and Owens, G.: Dataset characteristics influence the  
507 performance of different interpolation methods for soil salinity spatial mapping,  
508 *Environ. Monit. Assess.*, 191(11), 684, 2019.
- 509 Savtchenko, A.K., Huffman, G., and Vollmer, B.: Assessment of precipitation  
510 anomalies in California using TRMM and MERRA data, *J. Geophys. Res.:*  
511 *Atmos.*, 120(16), 8206-8215, 2015.
- 512 Shen, G., Chen, N., Wang, W., and Chen Z.: WHU-SGCC: a novel approach for  
513 blending daily satellite (CHIRP) and precipitation observations over the Jinsha  
514 River basin, *Earth Syst. Sci. Data*, 11(4), 1711-1744, 2019.
- 515 Shen, Y., Xiong, A., Wang, Y., and Xie, P.: Performance of high-resolution satellite  
516 precipitation products over China, *J. Geophys. Res.: Atmos.*, 115(D2), 2010.
- 517 Shen, Y., Zhao, P., Pan, Y., and Yu, J.: A high spatiotemporal gauge-satellite merged  
518 precipitation analysis over China, *J. Geophys. Res.: Atmos.*, 119(6), 3063-3075,  
519 2014.
- 520 Shi, P., Bai, X., Kong, F., Fang, J., Gong, D., Zhou, T., Guo, Y., Liu, Y., Dong, W.,  
521 Wei, Z., He, C., Yu, D., Wang, J., Ye, Q., Yu, R., and Chen, D.: Urbanization  
522 and air quality as major drivers of altered spatiotemporal patterns of heavy  
523 rainfall in China, *Landscape Ecol.*, 32(8), 1723-1738, 2017.





- 524 Smith, C.D., Yang, D., Ross, A., and Barr, A.: The Environment and Climate Change  
525 Canada solid precipitation intercomparison data from Bratt's Lake and Caribou  
526 Creek, Saskatchewan, *Earth Syst. Sci. Data*, 11(3), 1337-1347, 2019.
- 527 Su, F., Hong, Y., and Lettenmaier, D.P.: Evaluation of TRMM Multisatellite  
528 Precipitation Analysis (TMPA) and its utility in hydrologic prediction in the La  
529 Plata Basin, *J. Hydrometeorol.*, 9(4), 622-640, 2008.
- 530 Sun, Q., Miao, C., Duan, Q., Ashouri, H., Soroosh, S., and Hsu, K.: A review of  
531 global precipitation data sets: Data sources, estimation, and intercomparisons,  
532 *Rev. Geophys.*, 56(1), 79-107, 2018.
- 533 Tong, K., Su, F., Yang, D., and Hao, Z.: Evaluation of satellite precipitation retrievals  
534 and their potential utilities in hydrologic modeling over the Tibetan Plateau, *J.*  
535 *Hydrol.*, 519, 423-437, 2014.
- 536 Verma, K., and Katpatal, Y.B.: Groundwater monitoring using GRACE and GLDAS  
537 data after downscaling within basaltic aquifer system, *Groundwater*, 2019.
- 538 Wang, F., Wang, L., Koike, T., Zhou, H., Yang, K., Wang, A., and Li, W.: Evaluation  
539 and application of a fine-resolution global data set in a semiarid mesoscale river  
540 basin with a distributed biosphere hydrological model, *J. Geophys. Res.: Atmos.*,  
541 116(D21), 2011.
- 542 Wang, L., and Koike, T.: Comparison of a distributed biosphere hydrological model  
543 with GBHM, *Annual Journal of Hydraulic Engineering-JSCE*, 53, 103-108,  
544 2009a.
- 545 Wang, L., Koike, T., Yang, K., and Yeh, P.J.: Assessment of a distributed biosphere



- 546 hydrological model against streamflow and MODIS land surface temperature in  
547 the upper Tone River Basin, *J. Hydrol.*, 377(1-2), 21-34, 2009b.
- 548 Wang, L., Sun, L., Shrestha, M., Li, X., Liu, W., Zhou, J., Yang, K., Lu, H., and Chen,  
549 D.: Improving snow process modeling with satellite-based estimation of  
550 near-surface-air-temperature lapse rate, *J. Geophys. Res.: Atmos.*, 121(20),  
551 12005-12030, 2016.
- 552 Wang, L., Zhou, J., Qi, J., Sun, L., Yang, K., Tian, L., Lin, Y., Liu, W., Shrestha, M.,  
553 Xue, Y., Koike, T., Ma, Y., Li, X., Chen, Y., Chen, D., Piao, S., and Lu, H.:  
554 Development of a land surface model with coupled snow and frozen soil physics,  
555 *Water Resour. Res.*, 53(6), 5085-5103, 2017a.
- 556 Wang, S., Liu, J., Wang, J., Qiao, X., and Zhang, J.: Evaluation of GPM IMERG  
557 V05B and TRMM 3B42V7 Precipitation products over high mountainous  
558 tributaries in Lhasa with dense rain gauges, *Remote Sens.*, 11(18), 2080, 2019a.
- 559 Wang, Y., Chen, J., and Yang, D.: Bayesian assimilation of multiscale precipitation  
560 data and sparse ground gauge observations in mountainous areas, *J.*  
561 *Hydrometeorol.*, 20(8), 1473-1494, 2019b.
- 562 Wang, Y., Wang, L., Li, X., and Chen, D.: Temporal and spatial changes in estimated  
563 near-surface air temperature lapse rates on Tibetan Plateau, *Int. J. Climatol.*,  
564 38(7), 2907-2921, 2018.
- 565 Wang, Y., Wang, L., Li, X., and Zhou, J.: High temporal and spatial resolution  
566 precipitation data of Upper Brahmaputra River Basin (1981-2016), Zenodo,  
567 <http://doi.org/10.5281/zenodo.3711155>, 2020.



- 568 Wang, Y., Yang, H., Yang, D., Qin, Y., Gao, B., and Cong, Z.: Spatial Interpolation  
569 of Daily Precipitation in a High Mountainous Watershed based on Gauge  
570 Observations and a Regional Climate Model Simulation, *J. Hydrometeorol.*,  
571 18(3), 845-862, 2017b.
- 572 Xia, T., Wang, Z., and Zheng, H.: Topography and data mining based methods for  
573 improving satellite precipitation in mountainous areas of China, *Atmosphere*,  
574 6(8), 983-1005, 2015.
- 575 Xia, Y., Hao, Z., Shi, C., Li, Y., Meng, J., Xu T., Wu, X., and Zhang B.: Regional and  
576 Global Land Data Assimilation Systems: Innovations, Challenges, and Prospects,  
577 *J. Meteorol. Res.*, 33(2), 159-189, 2019.
- 578 Xia, Y., Mocko, D.M., Wang, S., Pan, M., Kumar, S.V., Peters-Lidard, C.D., Wei, H.,  
579 Wang, D., and Ek, M.B.: Comprehensive evaluation of the variable infiltration  
580 capacity (VIC) model in the North American Land Data Assimilation System, *J.*  
581 *Hydrometeorol.*, 19(11), 1853-1879, 2018.
- 582 Xu, R., Tian, F., Yang, L., Hu, H., Lu, H., and Hou, A.: Ground validation of GPM  
583 IMERG and TRMM 3B42V7 rainfall products over southern Tibetan Plateau  
584 based on a high-density rain gauge network, *J. Geophys. Res.: Atmos.*, 122(2),  
585 910-924, 2017.
- 586 Xue, B., Wang, L., Yang, K., Tian, L., Qin, J., Chen, Y., Zhao, L., Ma, Y., Koike, T.,  
587 Hu, Z., and Li, X.: Modeling the land surface water and energy cycles of a  
588 mesoscale watershed in the central Tibetan Plateau during summer with a  
589 distributed hydrological model, *J. Geophys. Res.: Atmos.*, 118(16), 8857-8868,



- 590           2013.
- 591   Yang, K., He, J., Tang, W., Qin, J., and Chen, C.C.K.: On downward shortwave and  
592           longwave radiations over high altitude regions: observation and modeling in the  
593           Tibetan Plateau, *Agr. Forest Meteorol.*, 150(1), 38-46, 2010.
- 594   Yang, K., Wu, H., Qin, J., Lin, C., Tang, W., and Chen, Y.: Recent climate changes  
595           over the Tibetan Plateau and their impacts on energy and water cycle: A review,  
596           *Global Planet. Change*, 112, 79-91, 2014.
- 597   Yi, X., Li, G., and Yin, Y.: Spatio-temporal variation of precipitation in the  
598           Three-River Headwater Region from 1961 to 2010, *J. Geogr. Sci.*, 23(3),  
599           447-464, 2013.
- 600   Yong, B., Liu, D., Gourley, J.J., Tian, Y., Huffman, G.J., Ren, L., and Hong, Y.:  
601           Global view of real-time TRMM multisatellite precipitation analysis:  
602           Implications for its successor global precipitation measurement mission, *Bull.*  
603           *Am. Meteorol. Soc.*, 96(2), 283-296, 2015.
- 604   Zaitchik, B.F., Rodell, M., and Olivera, F.: Evaluation of the Global Land Data  
605           Assimilation System using global river discharge data and a source-to-sink  
606           routing scheme, *Water Resour. Res.*, 46(6), 2010.
- 607   Zhang, Q., Shi, P., Singh, V.P., Fan, K., and Huang, J.: Spatial downscaling of  
608           TRMM - based precipitation data using vegetative response in Xinjiang, China,  
609           *Int. J. Climatol.*, 37(10), 3895-3909, 2017.
- 610   Zhou, J., Wang, L., Zhang, Y., Guo, Y., Li, X., and Liu, W.: Exploring the water  
611           storage changes in the largest lake (Selin Co) over the Tibetan Plateau during



612           2003–2012 from a basin-wide hydrological modeling, *Water Resour. Res.*,  
613           51(10), 8060-8086, 2015a.  
614   Zhou, Y., Lau, W.K.M., and Huffman, G.J.: Mapping TRMM TMPA into average  
615           recurrence interval for monitoring extreme precipitation events, *J. Appl.*  
616           *Meteorol. Clim.*, 54(5), 979-995, 2015b.  
617



618 **Table and figure captions**

619 **Table 1.** The precipitation products used in this study.

620 **Figure 1.** The Upper Brahmaputra River Basin originates from the Tibetan Plateau  
621 (TP) with the spatial distribution of nine meteorological stations from the China  
622 Meteorological Administration (CMA) and 166 rain gauges from Ministry of Water  
623 Resources (MWR), China. The green arrow indicates the direction of the westerlies,  
624 the Indian monsoon and the East Asian monsoon. The elevation data was obtained  
625 from the SRTM DEM datasets ([www.earthexplorer.usgs.gov](http://www.earthexplorer.usgs.gov)).

626 **Figure 2.** The flowchart used to produce the spatio-temporal continuous precipitation  
627 dataset ( $P_{int}$ ).

628 **Figure 3.** The spatial distribution of  $P_{int}$  (mm) averaged from 1981 to 2016 (a.  
629 annual; b. seasonal).

630 **Figure 4.** The spatial distribution of different precipitation products during the warm  
631 season (May to October) and the cold season (November to April) averaged from  
632 2008 to 2016.

633 **Figure 5.** Variations in basin-averaged precipitation from multi-year monthly mean  
634 values (top), annual values (middle) and monthly values (bottom) for the different  
635 products.

636 **Figure 6.** A comparison of the probability distribution function (PDF) between all the  
637 monthly observations and different precipitation products in the warm seasons (May  
638 to October in 2014 and 2016).

639 **Figure 7.** As for Figure 6 but with scatter plots.



640 **Figure 8.** A validation of  $P_{int}$  against short time series by comparing with daily  
641 gauge-averaged precipitation from May to October in 2014 and 2016.

642 **Figure 9.** A validation of  $P_{int}$  (mm) against short time series: spatial distribution of  
643 the observations and corresponding grids in  $P_{int}$  from May to October in 2014 and  
644 2016.

645 **Figure 10.** A validation of  $P_{int}$  against a long time series: (a). PDF and scatter plots  
646 for monthly precipitation at nine CMA stations, (b). station-averaged monthly  
647 precipitation from 1981 to 2016.

648 **Figure 11.** A trend analysis of the annual and seasonal precipitation (a: annual; b:  
649 spring; c: summer; d: autumn; e: winter) over 36 years (1981-2016) between  $P_{int}$ ,  
650 GLDAS, ITP-Forcing and MERRA2. The triangles represent the observed trend of  
651 the corresponding meteorological stations.

652 **Figure 12.** The number of meteorological stations (total of nine) which present the  
653 same trends as the different precipitation products, according to Figure 11.

654 **Figure 13.** A comparison of extreme events, as captured by different precipitation  
655 products.

656 **Figure 14.** An evaluation of simulated daily discharge at Nuxia station from 2008 to  
657 2016 forced by different precipitation products. All the discharge values have been  
658 normalized.

659



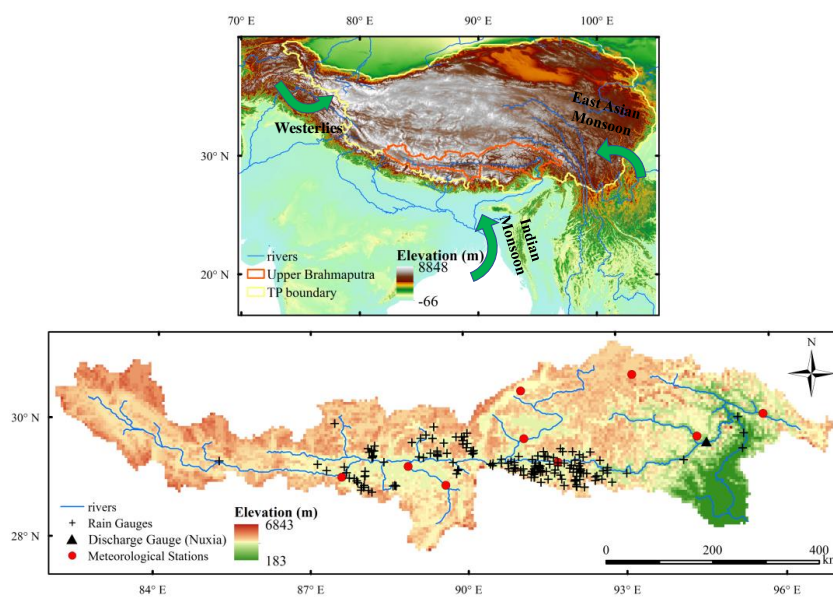
660 **Table 1.** The precipitation products used in this study.

Precipitation products	Time range	Temporal resolution	Spatial resolution
CMA gridded data	2008-2016	hourly	0.1°×0.1°
GLDAS	1981-2016	3-hour	0.25°×0.25°
ITP-Forcing	1981-2016	3-hour	0.1°×0.1°
MERRA2	1981-2016	hourly	0.5°×0.625°
TRMM	1998-2016	3-hour	0.25°×0.25°

661

662

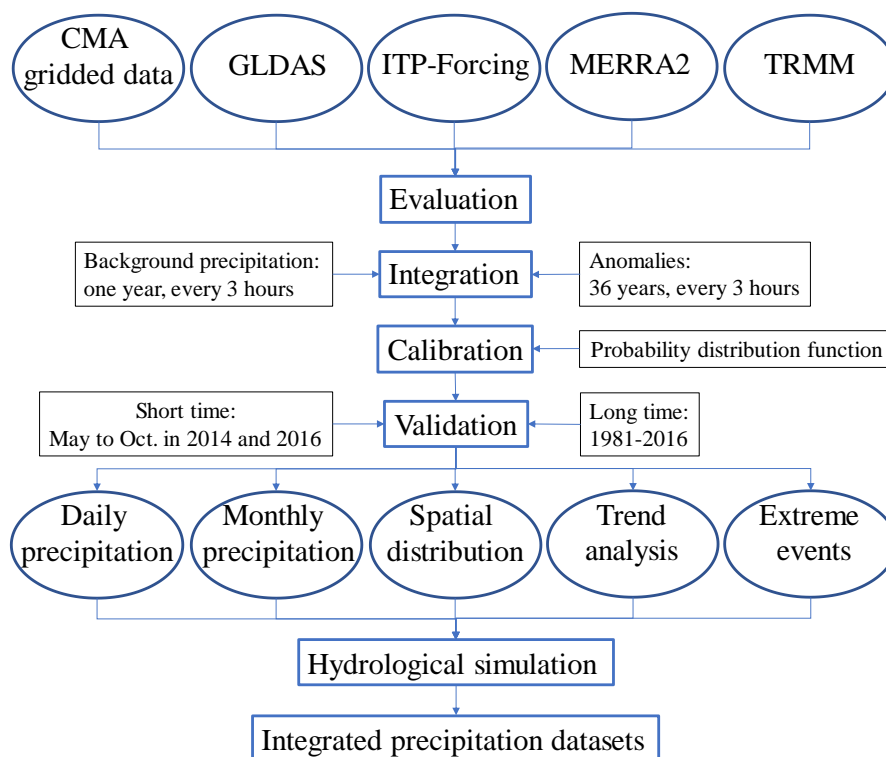




663

664 **Figure 1.** The Upper Brahmaputra River Basin originates from the Tibetan Plateau  
665 (TP) with the spatial distribution of nine meteorological stations from the China  
666 Meteorological Administration (CMA) and 166 rain gauges from Ministry of Water  
667 Resources (MWR), China. The green arrow indicates the direction of the westerlies,  
668 the Indian monsoon and the East Asian monsoon. The elevation data was obtained  
669 from the SRTM DEM datasets ([www.earthexplorer.usgs.gov](http://www.earthexplorer.usgs.gov)).

670

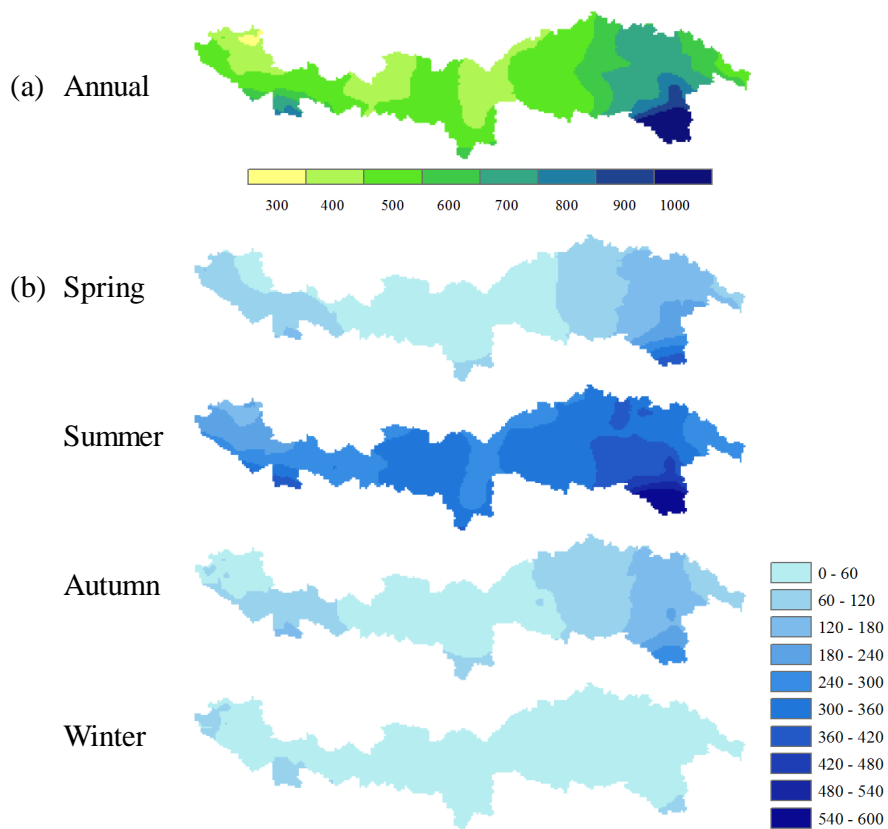


671

672 **Figure 2.** The flowchart used to produce the spatio-temporal continuous precipitation

673 dataset ( $P_{int}$ ).

674

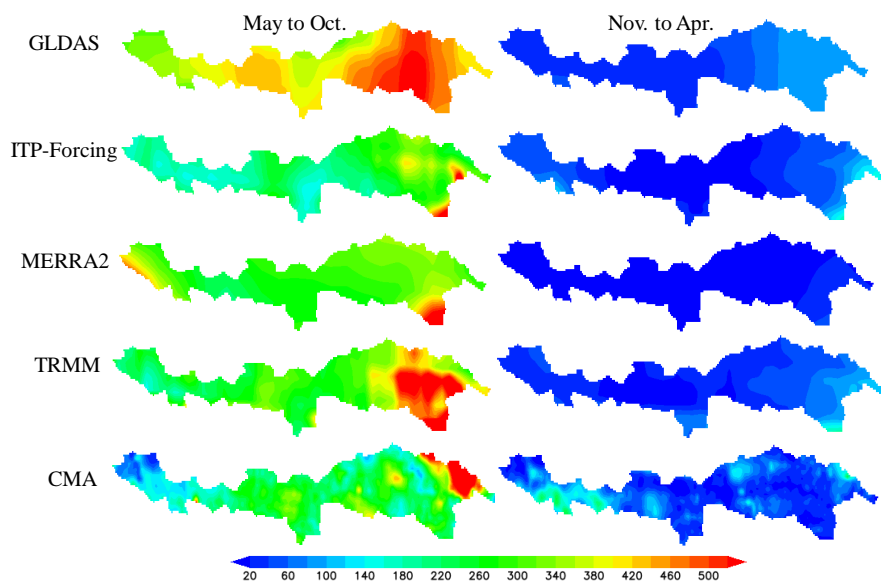


675

676 **Figure 3.** The spatial distribution of  $P_{int}$  (mm) averaged from 1981 to 2016 (a.

677 annual; b. seasonal).

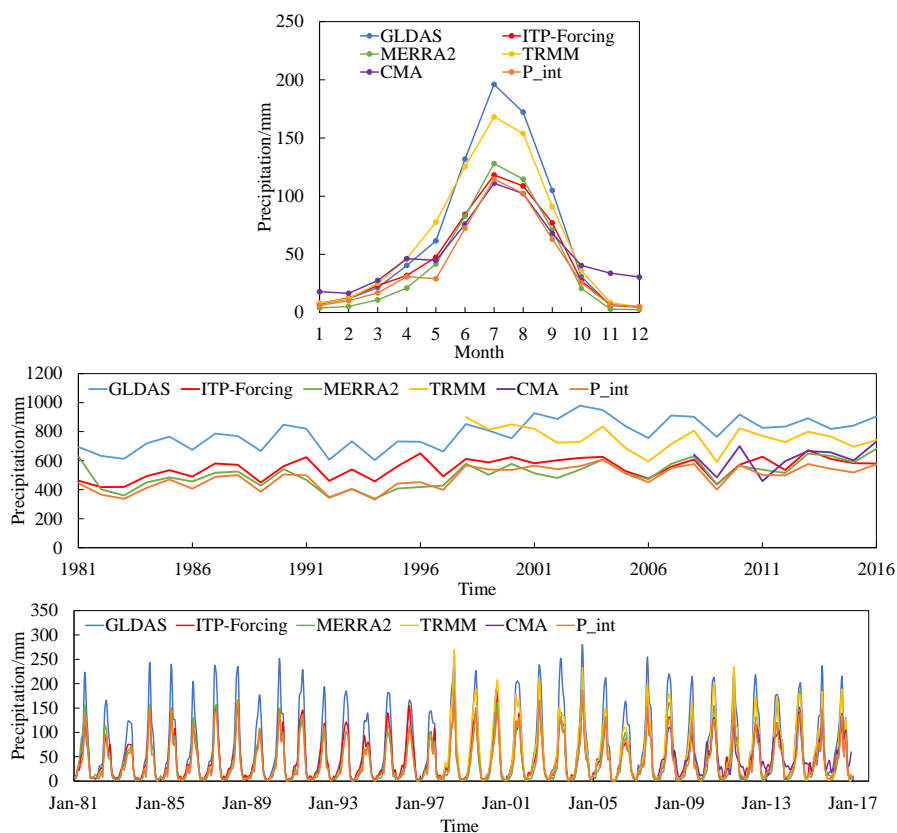
678



679

680 **Figure 4.** The spatial distribution of different precipitation products during the warm  
681 season (May to October) and the cold season (November to April) averaged from  
682 2008 to 2016.

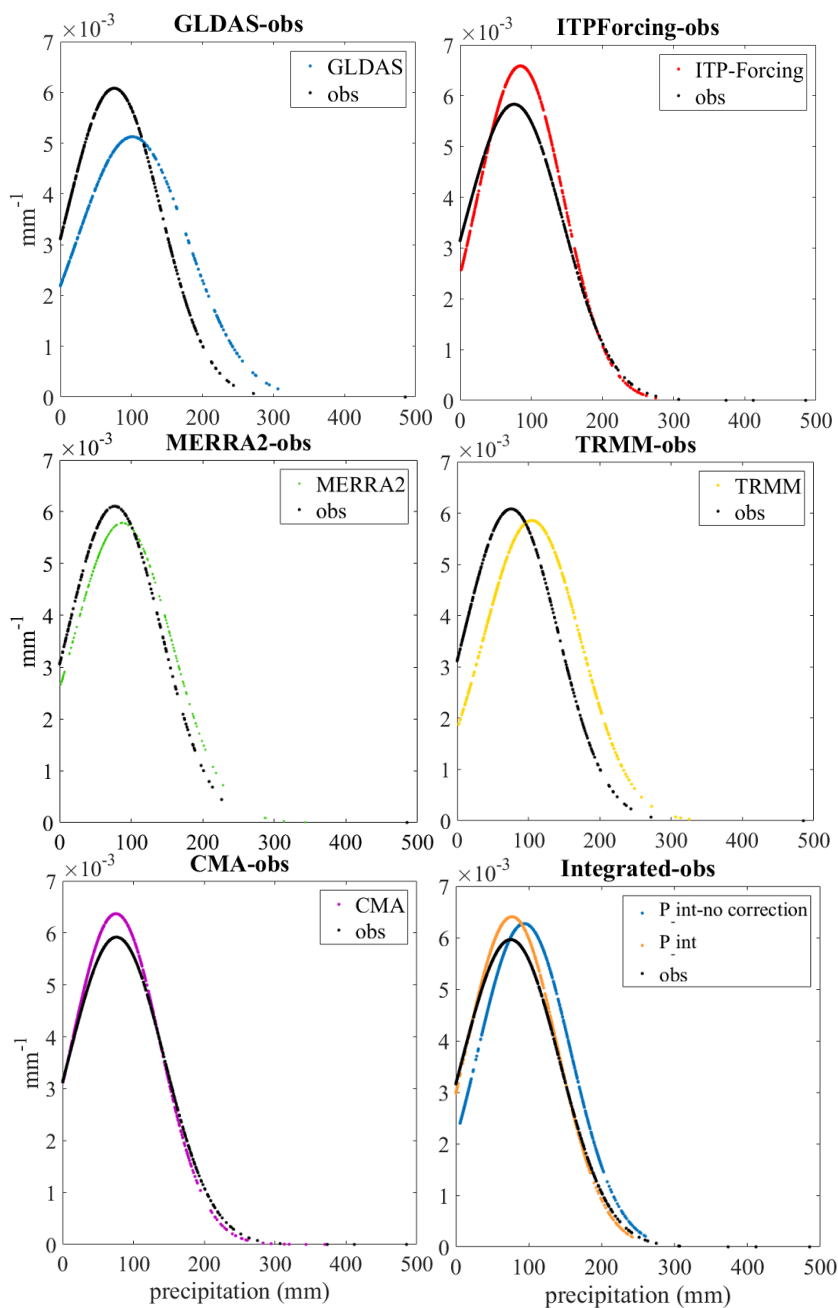
683



684

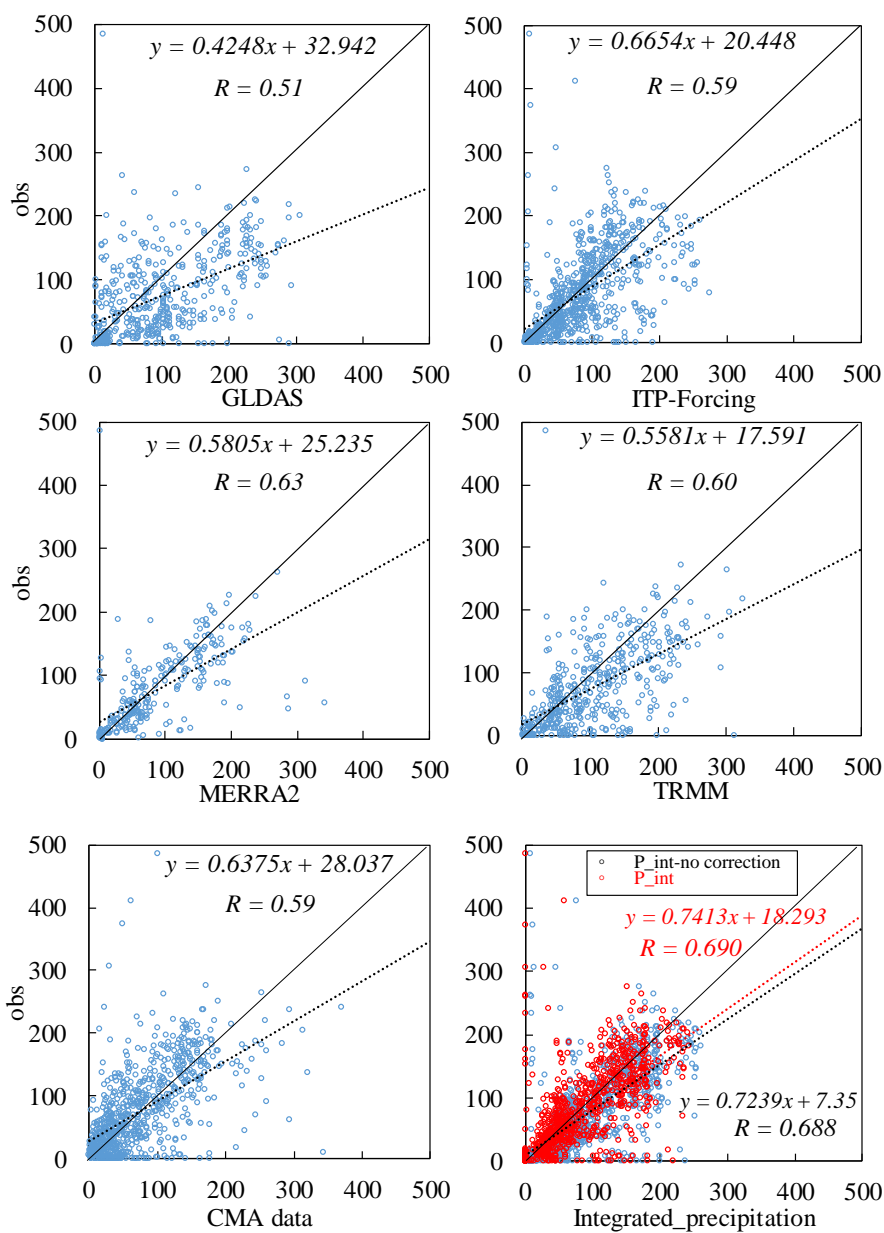
685 **Figure 5.** Variations in basin-averaged precipitation from multi-year monthly mean  
686 values (top), annual values (middle) and monthly values (bottom) for the different  
687 products.

688



689

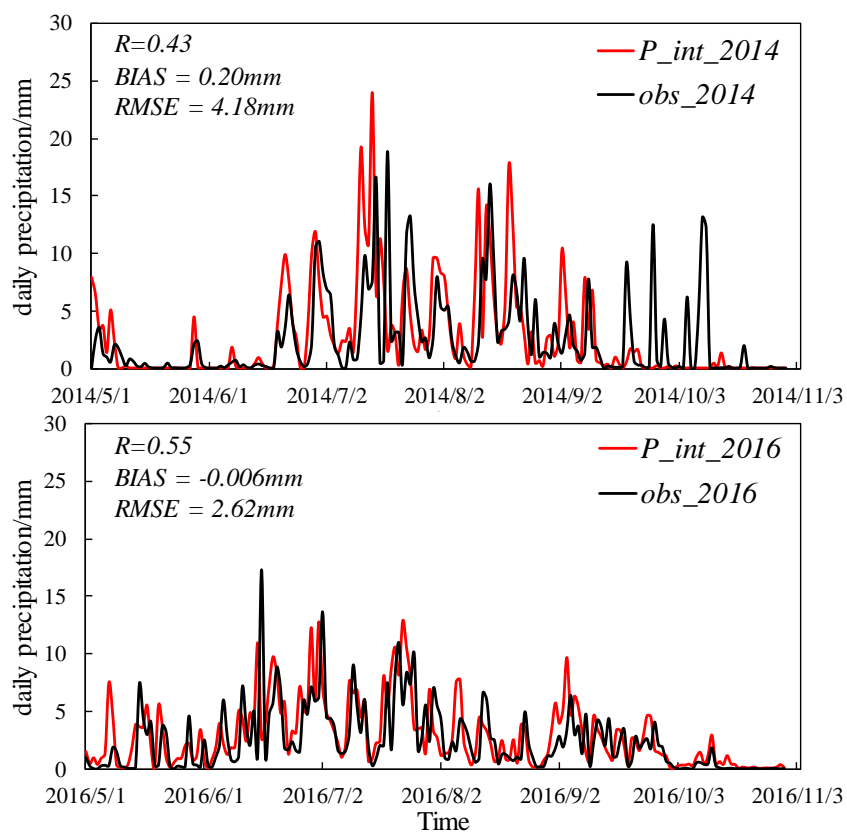
690 **Figure 6.** A comparison of the probability distribution function (PDF) between all the  
691 monthly observations and different precipitation products in the warm seasons (May  
692 to October in 2014 and 2016).



693

694

695 **Figure 7.** As for Figure 6 but with scatter plots.



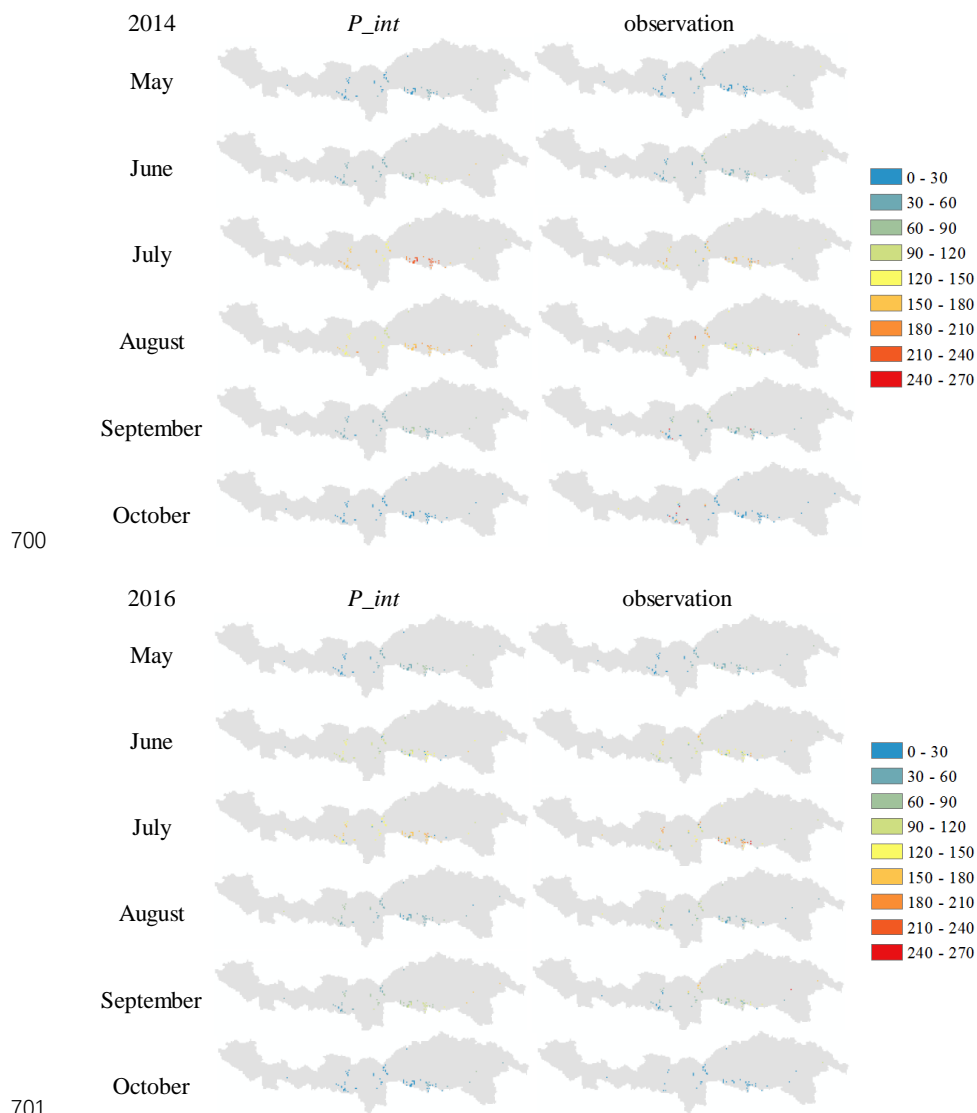
696

697 **Figure 8.** A validation of  $P_{int}$  against short time series by comparing with daily

698 gauge-averaged precipitation from May to October in 2014 and 2016.

699

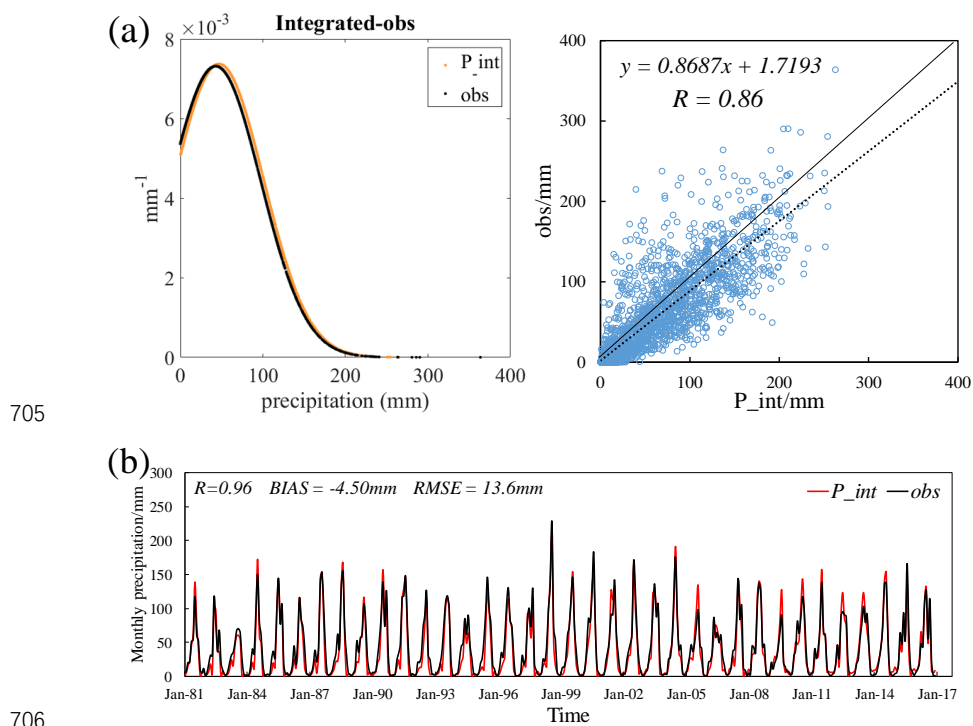




700

701

702 **Figure 9.** A validation of  $P_{int}$  (mm) against short time series: spatial distribution of  
703 the observations and corresponding grids in  $P_{int}$  from May to October in 2014 and  
704 2016.

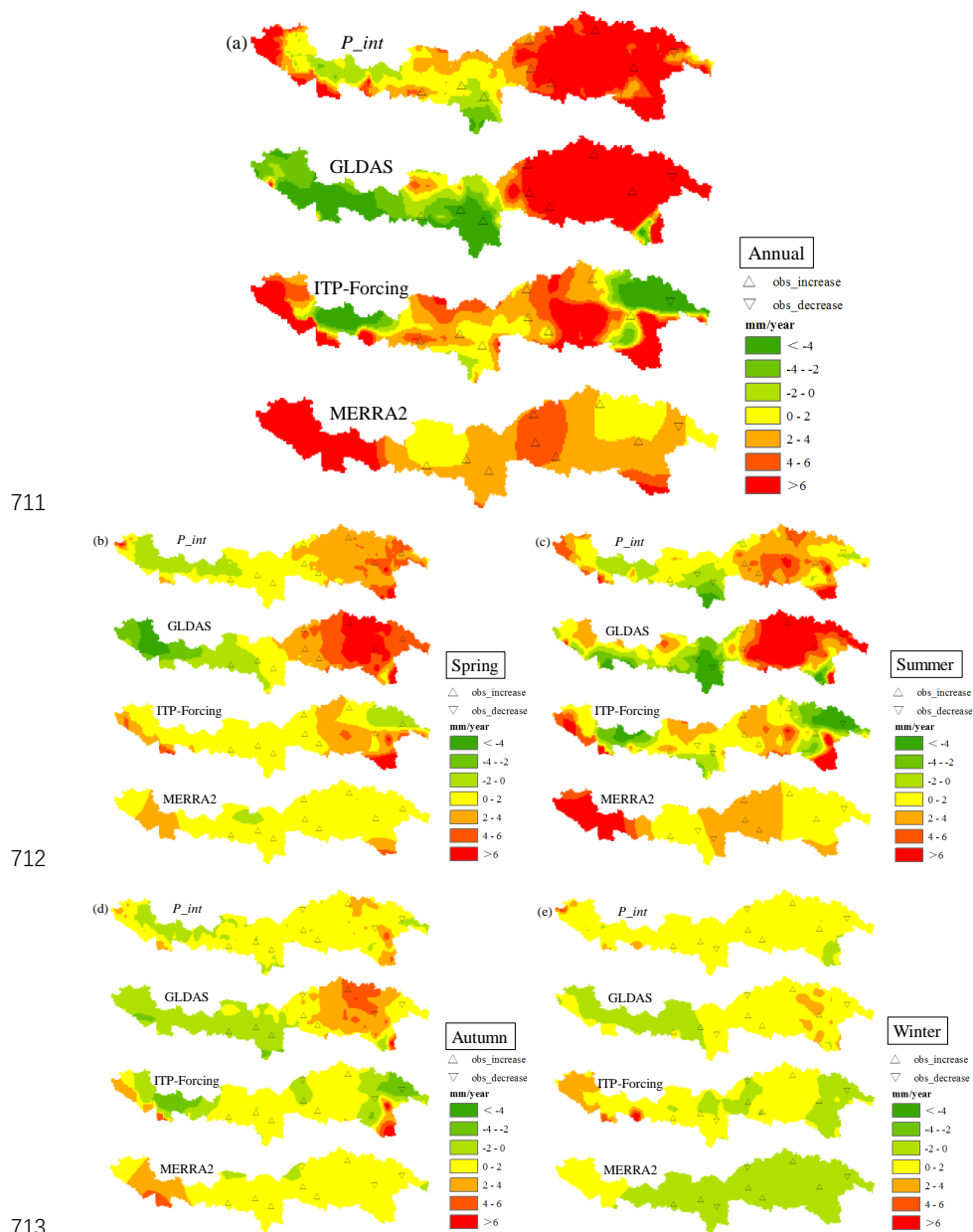


705

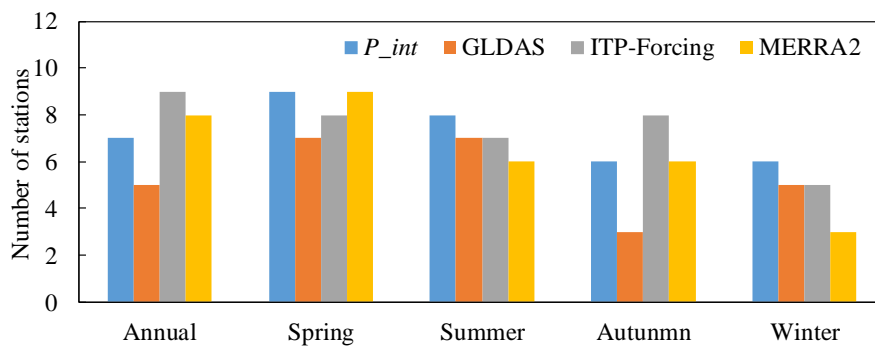
706

707 **Figure 10.** A validation of  $P_{int}$  against a long time series: (a). PDF and scatter plots  
708 for monthly precipitation at nine CMA stations, (b). station-averaged monthly  
709 precipitation from 1981 to 2016.

710



714 **Figure 11.** A trend analysis of the annual and seasonal precipitation (a: annual; b:  
715 spring; c: summer; d: autumn; e: winter) over 36 years (1981-2016) between  $P_{int}$ ,  
716 GLDAS, ITP-Forcing and MERRA2. The triangles represent the observed trend of  
717 the corresponding meteorological stations.

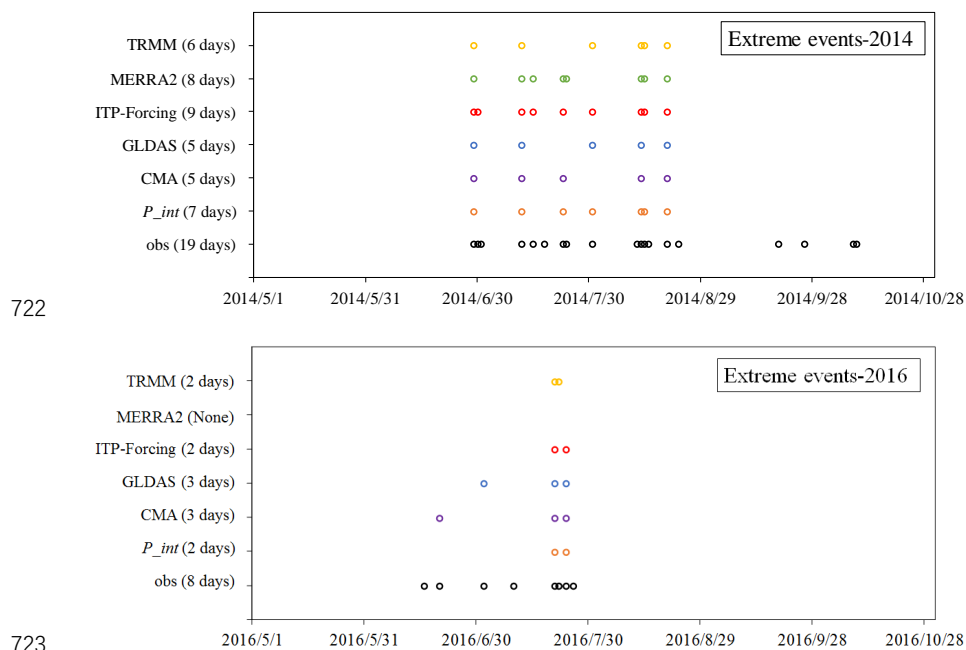


718

719 **Figure 12.** The number of meteorological stations (total of nine) which present the

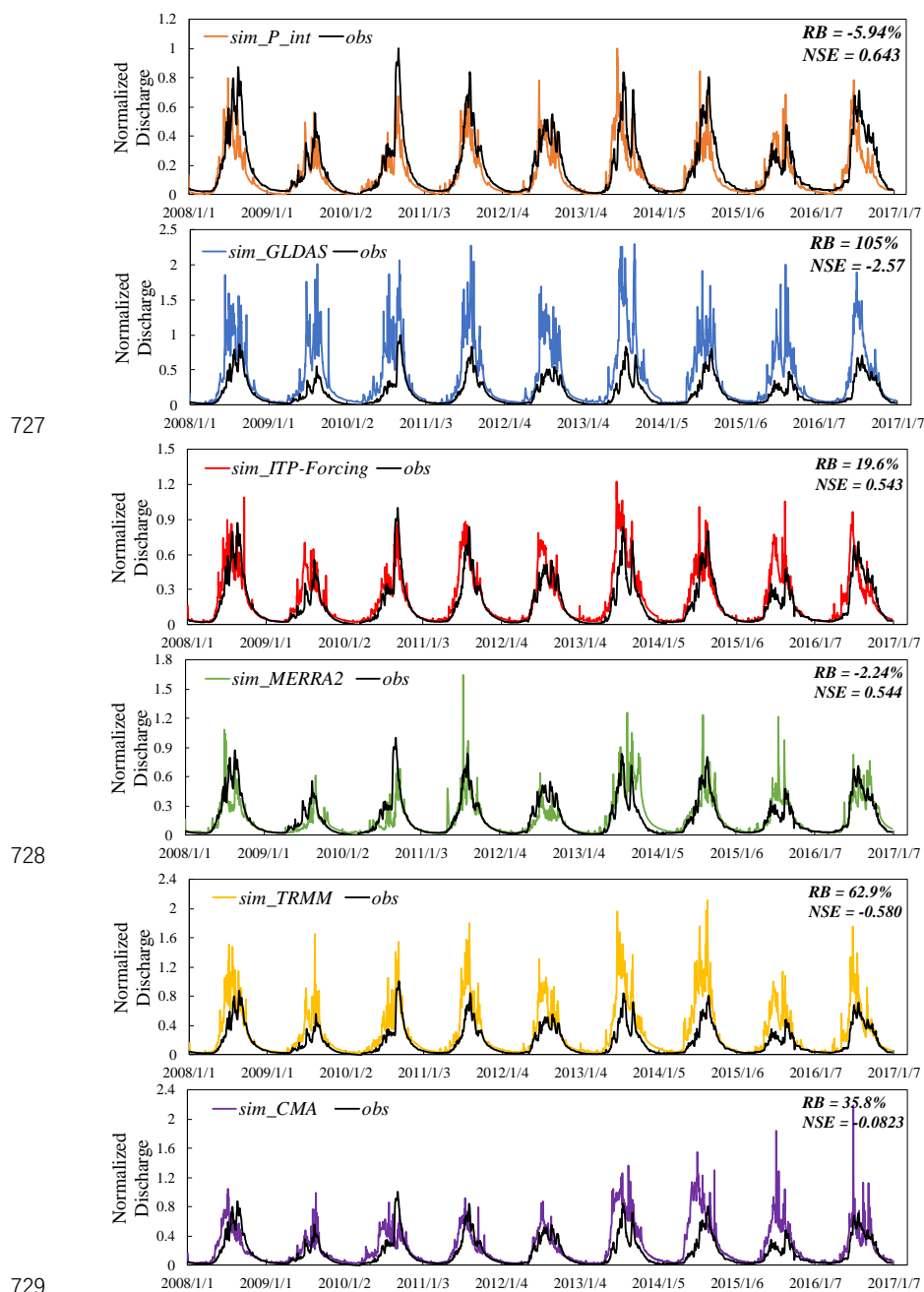
720 same trends as the different precipitation products, according to Figure 11.

721



724 **Figure 13.** A comparison of extreme events, as captured by different precipitation  
725 products.

726



727  
728  
729  
730 **Figure 14.** An evaluation of simulated daily discharge at Nuxia station from 2008 to  
731 2016 forced by different precipitation products. All the discharge values have been  
732 normalized.